Causes of hemispheric differences in polar cap indices

Lockwood, M. ORCID: https://orcid.org/0000-0002-7397-2172
(2023) Causes of hemispheric differences in polar cap indices. Journal of Atmospheric and Solar-Terrestrial Physics, 252. 106153. ISSN 1879-1824 doi: 10.1016/j.jastp.2023.106153
Available at https://centaur.reading.ac.uk/113670/

Journal of Atmospheric and Solar–Terrestrial Physics 252 (2023) 106153

Contents lists available at ScienceDirect

Journal of Atmospheric and Solar–Terrestrial Physics

journal homepage: www.elsevier.com/locate/jastp

Research paper

Causes of hemispheric differences in polar cap indices

M. Lockwood

University of Reading, Department of Meteorology, Earley Gate, Reading, RG6 6BB, Berkshire, United Kingdom

ARTICLE INFO

Dataset link: https://omniweb.gsfc.nasa.gov/ow_min.html, http://isgi.unistra.fr/data_download.php

Keywords:
Solar wind-magnetosphere coupling
Polar cap indices
Hemispheric differences
Annual variations
Universal time variations

ABSTRACT

Two recent papers by Troshichev et al. (2023) and by Lockwood (2023) have presented different physical mechanisms that cause simultaneous polar cap indices, measured close to the geomagnetic poles in the north and south hemispheres, to differ even though their overall behaviour is very similar. Several effects are described but the two main mechanisms discussed are the effect of the dawn–dusk (Y) component of the Interplanetary Magnetic Field (IMF) and inductive decoupling of electric fields caused by changes in the magnetic fields in the magnetosheath and magnetospheric lobes. This paper shows that both papers are correct and that both of the two major mechanisms are active and cause differences between the northern and southern indices. The variations in the differences with fraction of the calendar year and Universal Time are described and explained.

1. Introduction

1.1. Derivation and development of the Polar Cap Indices

The Polar Cap Indices (PCI) are generated using data from one magnetometer station in each hemisphere, each close to the geomagnetic pole (Stauning, 2021a,b; Troshichev, 2022). The northern hemisphere index, PCN, is derived from observations made at Thule (Qaanaaq) in Greenland and the southern hemisphere index, PCS, is derived from observations made at Vostok in Antarctica. These stations are not precisely at the geomagnetic poles and do not have exactly the same relationship to the nearby pole. Indeed, the magnetic pole locations depend on the definition adopted, the field model employed and the date because the magnetic poles (of all definition) have drifted with changes in the intrinsic geomagnetic field (Lockwood, 2023).

The PCN and PCS indices are derived from enhancements of the horizontal magnetic field components relative to the quiet level observed at the two stations. The effects of ionospheric conductivity variations are partially allowed for by taking the difference with respect to a quiet-day reference and Troshichev and Andrezen (1985) showed the resulting index correlated highly with the coupling function E_{KL}, which was derived from *in-situ* observations of interplanetary parameters by Kan and Lee (1979) who regarded it as an estimate of E_m, the reconnection rate (the electric field along the reconnection X-line) in the dayside magnetopause. The theory of the derivation of the PCI was also explicitly based on the idea that E_{KL} was an estimate of the reconnection rate (e.g., Stauning, 2013). Note also that the regression with E_{KL} means that the PCI, despite being intrinsically magnetic field observations, are given in units of mV m^{-1}. Subsequently, Borovsky and Birn (2014) made the point that there is no simple relationship between E_{KL} and E_m. There are two main reasons for this. (1) The magnetic flux in a flux tube is, by definition, constant and equal to $\pi\delta^2 B/4$ where and B is the magnetic field and δ is the diameter of the tube. Hence B varies along the flux tube as $\delta^{-1/2}$. In steady-state ($dB/dt = 0$), the voltage across a magnetic flux tube (the flux transfer rate) is constant along the length of the tube (otherwise $\nabla\cdot\vec{B} = 0$ is violated) and so $E\delta$ is constant, where E is the electric field which therefore varies as δ^{-1}. Hence in steady state E varies as $B^{-1/2}$. Because the spatial variation of B of a reconnecting flux tube in the magnetosheath (between the bow shock and the reconnection X-line), E_{KL} and E_m are not the same and this spatial variation can be different in different steady-state situations. (2) There are also induction effects caused by temporal changes in the magnetic field that make E_{KL} and E_m differ according to Faraday's law: a non-zero ($d\vec{B}/dt$), means there is a curl of $\vec{E}$ and integrated along the flux tube in the magnetosheath this decouples E_{KL} and E_m. The formula of Kan and Lee (1979) computes the electric field in interplanetary space, E_{KL}, and so is better regarded as an empirical coupling function that correlates well with the PCI rather than an estimate of the actual reconnection electric field.

The method used to derive the indices allows for the effect of local ionospheric conductivity on the field deflections observed by the magnetometers at the two stations and this effect will usually be different in the two hemispheres because of the different solar zenith angles. This procedure has been shown to remain valid throughout solar cycles 23 and 24 by Troshichev et al. (2022a).

The southern hemisphere PCI, PCS, has been generated by the Arctic and Antarctic Research Institute (AARI) in St. Petersburg, and

E-mail address: m.lockwood@reading.ac.uk.
URL: http://www.personal.reading.ac.uk/~ym901336/index.html.

https://doi.org/10.1016/j.jastp.2023.106153
Received 16 July 2023; Received in revised form 14 October 2023; Accepted 16 October 2023
Available online 18 October 2023

the northern hemisphere index PCN by the Danish Meteorological Institute (DMI) and the Danish Space Research Institute (DTU Space) in Copenhagen. Both indices have been generated in a variety of versions over the years. Initially these indices were of 15 min resolution but the change to 1 min values was completed for both stations by 1999. It was found that there were both systematic and regular episodic inconsistencies between the PCN and PCS values (Lukianova et al., 2002; Ridley and Kihn, 2004). Such differences called for a unified method to be used to generate PCN and PCS to eliminate any influence of the calculation technique on results of the analysis. Hence, the unified method of PC index derivation, based on procedure used at AARI, was proposed by Troshichev et al. (2006) and implemented at AARI for PCS generation, but this method has not been adopted at DMI for PCN.

Because of the concern about differences between PCN and PCS, in 2009 the working group *DAT* of Division 5 of IAGA (the International Association of Geomagnetism and Aeronomy), *V-DAT*, appointed a Task Force to look into the issue. This team analysed three submitted PCI analysis procedures: (1) the "unified method" (Troshichev et al., 2006), (2) the official DMI method (Vennerstrøm, 1991) and (3) the "Solar Rotation Weighted" (SRW) method, suggested by Stauning (2011). Of these three, the Task Force selected method (1) for IAGA endorsement (see McCreadie and Menvielle, 2010).

The adoption of the PCI indices (generated by the unified method) by IAGA was initially recommended in 2013 (Menvielle et al., 2013) and endorsed at the XXII Assembly of IAGA at Merida, Mexico on August 25–31, 2013 (Resolution #3, 2021; see http://www.iaga-aiga.org/resolutions). In 2014 both the PCN and PCS indices for all previous years were recalculated with application of the unified method (Method 1) and the required three calibration parameters (α, β and ϕ) obtained for the full cycle of solar activity (1995–2005) (Matzka and Troshichev, 2014).

According to the IAGA rules, all indices are initially considered as "provisional". They should then be checked, making allowance for all possible faults (observational, technical and processing), to produce the "definitive" indices, which should be valid in perpetuity. This work was fulfilled at AARI and DTU Space in 2021 (Nielsen and Willer, 2019). Comparison of the PCN and PCS indices for 24 years (1997–2020) has demonstrated almost perfect agreement between the definitive indices and only a small number of differences between the series of provisional and definitive PCI indices. Consequently, the definitive PCN and PCS indices were finally approved by IAGA in 2021 and the indices were recommended for use by the international scientific community (IAGA Resolution #2, 2021; see https://www.iaga-aiga.org/resolutions/resolution-no-2-2021-polar-cap-pc-index/). A more detailed review of the development of the PCI has been given by Troshichev (2022).

The provisional and definitive PCI data can be retrieved from the International Service of Geomagnetic Indices (ISGI) from https://isgi.unistra.fr/geomagnetic_indices.php. It is certainly true that considerably greater agreement between PCS and PCN exists in the IAGA-approved version of the data than used to be the case before application of the unified method and other corrections and developments.

1.2. Physical causes of differences between PCN and PCS

Two recent papers by Stauning (2022a,b) have looked at differences between simultaneous definitive values of the PCN and PCS and attributed them to processing errors in PCS. On the other hand, Troshichev et al. (2022b, 2023) and Lockwood (2023) argue these differences are physical in origin and neither PCN nor PCS is invalid. Lockwood (2023) has shown that not only are the distributions of definitive PCN and PCS almost identical, but also the distributions of $(PCN - E_{KL})$ and $(PCS - E_{KL})$ are equally close to identical. Hence neither PCN nor PCS can be considered to be more in error than the other. This highlights the relevance of E_{KL} being considered as an empirical coupling function rather than the electric field along the reconnection line, E_m: the point being that in steady-state (i.e. without temporal changes in the magnetospheric magnetic field causing induction effects) the electric field in both polar caps would be equal to the mapped value of E_m and this leads to the incorrect idea that PCN and PCS should always be similar.

Troshichev et al. (2023) have looked at how non-zero values of $(PCN - PCS)$ are induced by the Y-component of the Interplanetary Magnetic Field (IMF) through its effect on the dawn–dusk distribution of F-region flows and the associated "DP-4" (Disturbance Polar 4) current system in the E-region ionosphere. Lockwood (2023) discussed a number of different physical mechanisms that cause instantaneous values of PCN and PCS to differ but showed that their overall behaviour is very similar. A key part of the discussion in the paper by Lockwood (2023) is inductive decoupling of electric fields caused by changes in the magnetic field in the magnetosheath and magnetospheric lobes. Both these papers also noted the effect of ionospheric conductivities and how the tilt of Earth's magnetic axis introduces systematic daily and annual variations. In addition, differences between PCN and PCS can be caused by transient bursts of enhanced EUV and X-ray photoionization caused by solar flares and/or due to particle precipitation ionization by SEP (Solar Energetic Particle) events, particles that are accelerated at shock fronts ahead of CMEs (Coronal Mass Ejections) as they propagate through the heliosphere.

2. Data employed in this study

The PCI data for both hemispheres used here are derived from data recorded between 1 January 1998 to 31 December 2018 (i.e.,1998–2018, inclusive) that are available from the International Service for Geomagnetic Indices (ISGI). These data were downloaded on 11 February 2023 as annual ASCII files. For these years the data for both hemispheres are classed as "definitive" by ISGI, in accordance with IAGA procedures. As discussed in the previous section, neither PCN nor PCS should be considered as "in error" purely on the basis that one differs from the other. This is the same dataset as was employed by Lockwood (2023). The study by Troshichev et al. (2023) included data for 2019–2021, which are also available from ISGI, with the PCN data classed as definitive for 2019 and 2020 and "provisional" for 2021 and the PCS classed as provisional for all three of these years. The entire study presented here was also carried out including these three years (i.e. for 1998–2021, inclusive) and results were essentially identical to those reported here.

One technical detail to note is that a number of the PCS data records downloaded from ISGI contain a rogue 99 999 added to the minutes field. As in the study by Lockwood (2023), these records are here treated as bad data. In addition, some other records are missing in the PCS data series, including all data for 2003. As a result, the 1998–2018 (inclusive) dataset contains 11,028,946 1-min PCN samples, and 10,337,662 1-min PCS samples out of a possible 11,044,800. The number of simultaneous PCN and PCS samples is 10,337,561.

In addition to these PCI data, this paper also makes use of IMF and solar wind data that were downloaded from the OMNI dataset (King and Papitashvili, 2005), available from the Space Physics Data Facility (SPDF) at NASA's Goddard Space Flight Center. These data have been lagged to the nose of Earth's bow shock using a procedure that is good for hourly data but does cause some non-physical time sequences in 1-min data. These data have been further lagged using the optimum time lags, δt, between changes in the OMNI data and the response in the PCI, derived by Lockwood (2023). For the one-minute data the optimum lag was shown to be $\delta t = 19 \pm 4$ min whereas for hourly means a lag of 37 min (+36/−31) was derived.

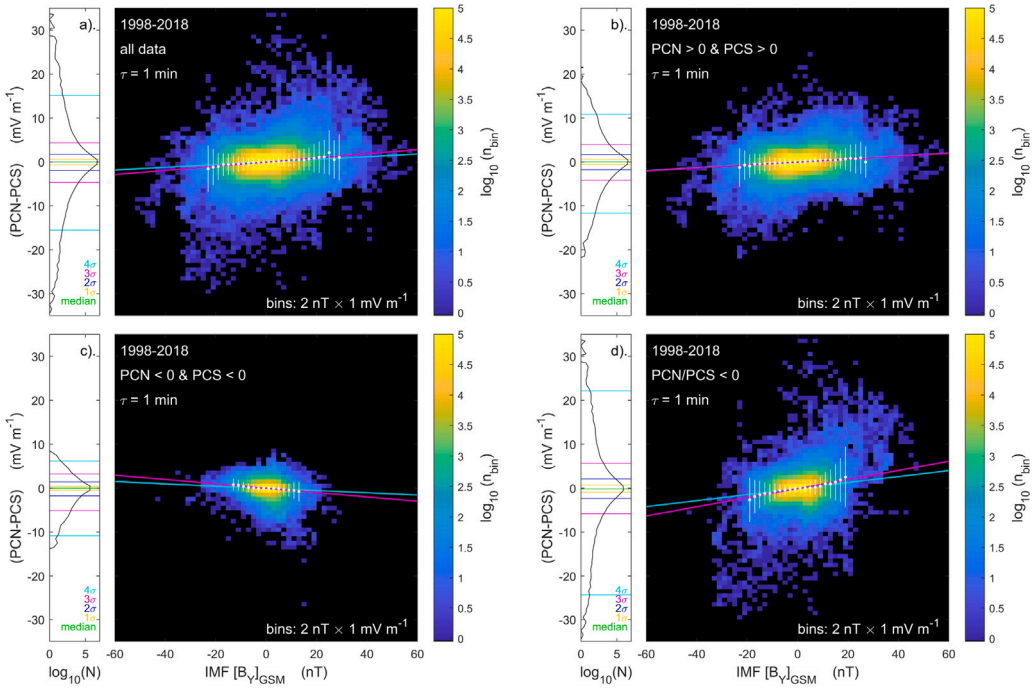

Fig. 1. Analysis of the effect of the Y-component of the Interplanetary Magnetic Field, IMF, in the GSM frame of reference ($[B_Y]_{GSM}$) on the difference between the Polar Cap Indices, ($PCN - PCS$), for 1-min data ($\tau = 1$ min). Four pairs of plots are presented for: (a) all data (1998–2018); (b) when both PCN and PCS are positive; (c) when both PCN and PCS are negative; and (d) when PCN and PCS have opposite polarities. The right-hand plot of each pair is a "data density plot" (two dimensional histogram) in which the logarithm (to base 10) of the number of samples in each bin, n_{bin}, is colour coded for bins that are 2 nT wide in $[B_Y]_{GSM}$ and 1 mV m^{-1} wide in ($PCN - PCS$). The white dots are the mean values in the 2 nT-wide $[B_Y]_{GSM}$ bins (with error bars plus and minus one standard deviation) and the cyan and mauve lines are linear regression fits to the raw 1 min and binned data, respectively. The left-hand plots of the pairs give the distributions of ($PCN - PCS$) values (on a log scale), the coloured lines marking the median, $\pm1\sigma$, $\pm2\sigma$, $\pm3\sigma$, and $\pm4\sigma$ points of the distribution.

3. The effect of the Y-component of the IMF on ($PCN - PCS$)

Fig. 1 looks at the dependence of 1-min ($PCN - PCS$) values on the IMF Y component in the Geocentric Solar Magnetospheric (GSM) frame, $[B_Y]_{GSM}$, using the optimum lag of $\delta t = 19$ min. Because the numbers of data samples is so high, a traditional scatter plot contains only information on the extreme outliers, all other points being so over-plotted that they merge into one black area. Hence this paper employs "data density plots" (two-dimensional histograms), in which the logarithm of the number of data pairs in each bin, n_{bin}, is colour-coded. In Fig. 1, the bins used are 2 nT wide in $[B_Y]_{GSM}$ and 1 mV m^{-1} wide in ($PCN - PCS$). The colour scale is chosen so that the 1-count level ($log_{10}(n_{bin}) = 0$) is the just above the blue/black transition and so the outliers can be seen in blue and empty bins are coloured black. However, unlike a scatter plot of so many data points, we can also see where most samples are. To the left of each data density plot is the distribution of the ($PCN - PCS$) values (on a logarithmic scale) on which the median and the $\pm1\sigma$, $\pm2\sigma$, $\pm3\sigma$, and $\pm4\sigma$ points of the distribution are marked by horizontal coloured lines.

Fig. 1 is divided into 4 parts: (a) is for all data; (b) is for positive values of both PCN and the simultaneous PCS; (c) is for negative values of both PCN and PCS; and (d) is for when PCN and PCS have the opposite polarity. A similar division was employed by Troshichev et al. (2023). Table 1 gives the numbers of simultaneous data pairs, N contributing to each part.

The cyan line on each data-density plot is a linear regression fit to all the 1-min samples. The slope s and intercept c of this regression line and the associated correlation coefficient R (along with the p-value p of the null hypothesis that $R = 0$) and the root-mean-square (r.m.s) fit residual, Δ_{rms} are all given in Table 1. Also given is the "adjusted R^2" value, R^2_{adj}. This is a goodness-of-fit metric for linear models. It identifies the fraction of the variance in that is explained by the regression line. R^2_{adj} differs from the coefficient of determination, R^2 because it has been adjusted for the number of predictors in the model.

$$R^2_{adj} = 1 - (1 - R^2) \times \frac{(N-1)}{(N-k-1)} \quad (1)$$

where N is the number of samples and k is the number of independent variables in the model, excluding the constant.

One problem with linear regression is that it is dominated by the high weighting of so many samples near the means of the distributions (Barnett, 2004; Lockwood et al., 2006b; Sivadas and Sibeck, 2022). To check for this, I here use the method used by Vasyliunas et al. (1982) and Lockwood and McWilliams (2021a) to ensure the extremes are not under-weighted in the fit: the data are averaged into bins of $[B_Y]_{GSM}$ that cover the whole range and then these treated with equal weight and fitted. The white dots are the means in bins 2 nT wide with error bars that are plus and minus one standard deviation. Because the linear fit residuals increase dramatically if the number of samples in a bin falls below 500, only means of more than 500 samples are used. The mauve line is the regression fit to these mean values. Where mauve and cyan lines are similar or the same (for example in part (b) of Fig. 1), there is little or no effect of the weighting towards the mean.

Fig. 1 shows that ($PCN - PCS$) increases with $[B_Y]_{GSM}$ in all cases except when both PCN and PCS are negative (part c) when the opposite is true. The largest scatter is when PCN and PCS have opposite polarities (part d) and this gives the largest outliers in the all-data plot (part a). The numbers of samples N in the four categories given in Table 1 show that negative values (sunward convection) in both polar caps is rare, with sunward convection in just one polar cap (part d) being more than twice as common. Note also that positive values in both polar caps is more than twice as common as times when there is sunward convection seen in at least one polar cap. This is consistent with the PCI behaviour surveyed by Lockwood (2023).

An important metric in Table 1 is R^2_{adj} which quantifies the fraction of the variation in ($PCN - PCS$) that is explained by $[B_Y]_{GSM}$. That

Table 1
Correlations between $(PCN - PCS)$ and the Y-component of the IMF in the GSM frame, $[B_Y]_{GSM}$ for 1-min samples (τ = 1 min) and a propagation lag δt = 19 min and for data averaged in bins $2nT$ wide in $[B_Y]_{GSM}$.

Dataset	All data	PCN > 0, PCS > 0	PCN < 0, PCS < 0	PCN/PCS < 0
Figure	1a	1b	1c	1d
1-MINUTE DATA				
Number of samples, N	9,323,665	6,747,922	825,537	1,825,520
correlation coefficient, R	0.166	0.171	−0.103	0.228
p-value for null hypothesis, p	$<10^{-20}$	$<10^{-20}$	$<10^{-20}$	$<10^{-20}$
adjusted R^2, R^2_{adj}	0.027	0.029	0.011	0.052
r.m.s. fit residual, Δ_{rms} (mV m^{-1})	0.027	0.029	0.011	0.052
regression slope[a] s (10^{-3} mV m^{-1} nT^{-1})	36.24 ± 0.07	33.17 ± 0.07	−25.45 ± 0.27	36.24 ± 0.07
regression intercept[a] c (10^{-3} mV m^{-1})	−21.48 ± 0.29	4.66 ± 0.31	−21.48 ± 0.29	−46.76 ± 8.24
BINNED DATA[b]				
number samples, N	27	26	14	20
correlation coefficient, R	0.938	0.920	−0.963	0.971
p-value for null hypothesis, p	5.53×10^{-13}	2.81×10^{-11}	3.42×10^{-8}	1.32×10^{-12}
adjusted R^2 for binned data, R^2_{adj}	0.875	0.841	0.921	0.939
r.m.s. fit residual, Δ_{rms} (mV m^{-1})	0.283	0.221	0.121	0.311
regressions slope[a], s (10^{-3} mV m^{-1} nT^{-1})	47.21 ± 3.50	33.37 ± 2.89	−49.44 ± 4.00	103.58 ± 6.03
regression intercept[a], c (10^{-3} mV m^{-1} nT^{-1})	41.04 ± 55.48	−48.97 ± 4.38	−24.17 ± 32.21	−111.78 ± 69.59

[a] Linear regression fit $(PCN - PCS)_{fit} = s[B_Y]_{GSM} + c$.
[b] 2 nT-wide bins in $[B_Y]_{GSM}$.

Table 2
Correlations between (PCN-PCS) and the Y-component of the IMF in the GSM frame, $[B_Y]_{GSM}$ for 1-h averages (τ = 1 h) and lag δt = 37 min.

Dataset	All data	PCN > 0, PCS > 0	PCN < 0, PCS < 0	PCN/PCS < 0
Figure	3a	3b	3c	3d
1-HOUR DATA				
Number of samples, N	162,538	122,285	11,774	28,483
correlation coefficient, R	0.184	0.196	−0.113	0.230
p-value for null hypothesis, p	$<10^{-20}$	$<10^{-20}$	$<10^{-20}$	$<10^{-20}$
adjusted R^2, R^2_{adj}	0.034	0.038	0.013	0.053
r.m.s. fit residual, Δ_{rms} (mV m^{-1})	0.780	0.722	0.668	1.010
regression slope[a] s (10^{-3} mV m^{-1} nT^{-1})	38.28 ± 0.51	36.53 ± 0.52	−27.60 ± 2.24	65.29 ± 1.64
regression intercept[a] c (10^{-3} mV m^{-1})	−21.19 ± 1.93	5.15 ± 2.07	27.03 ± 6.20	−130.68 ± 5.98
BINNED DATA[b]				
number samples, N	24	24	11	16
correlation coefficient, R	0.981	0.985	−0.939	0.964
p-value for null hypothesis, p	4.12×10^{-17}	2.70×10^{-18}	1.82×10^{-5}	1.91×10^{-5}
adjusted R^2 for binned data, R^2_{adj}	0.063	0.969	0.869	0.924
r.m.s. fit residual, Δ_{rms} (mV m^{-1})	0.960	0.053	0.027	0.069
regressions slope[a], s (10^{-3} mV m^{-1} nT^{-1})	44.00 ± 1.87	42.14 ± 1.57	−21.24 ± 2.59	50.72 ± 3.74
regression intercept[a], c (10^{-3} mV m^{-1} nT^{-1})	17.96 ± 12.91	9.59 ± 10.88	−33.52 ± 8.30	−154.86 ± 17.23

[a] Linear regression fit $(PCN - PCS)_{fit} = s[B_Y]_{GSM} + c$.
[b] 2 nT-wide bins in $[B_Y]_{GSM}$.

fraction is lowest for the $PCN < 0$, $PCS < 0$ case (0.011) and highest for the mixed-polarity case (0.052) and between the two (0.029) for the $PCN > 0$, $PCS > 0$ case. This means that the IMF $[B_Y]$ effect, as found by Troshichev et al. (2023) is undoubtedly real and contributes typically 3% of the difference between simultaneous 1-min samples of PCN and PCS. Note that when we average the data, as in the binned dataset, the R^2_{adj} values rise to between 0.84 and 0.94 and so then we are averaging out most of the other effects that give of order 97% of the variation in the 1-min values (such as propagation lag errors, spatial structure in the IMF and observation noise).

Fig. 2 gives a representation of what these R^2_{adj} values mean in terms of the distributions of values. The black lines are the distributions of observed values of $(PCN - PCS)$ in the four subsets used in Fig. 1. The mauve and cyan lines are the distributions predicted by the distribution of $[B_Y]_{GSM}$ values, scaled using the two linear regression fits. Note the distributions are normalized by the total number of samples and the vertical axis scale is different in each panel. The double peaks in some of the scaled $[B_Y]_{GSM}$ distributions are because the regression lines does not quite pass through the mode of the distribution. The figure shows the observed distribution is always wider especially in cases for which R^2_{adj} is low.

At least some of the additional variability in $(PCN - PCS)$ in these 1-min values will be because of the variability in the true propagation lag around the optimum value of δt of 19 min. To look at this, the analysis was repeated for hourly averages, for which the optimum lag is 37 min Lockwood (2023). The results are shown in Fig. 3 and Table 2. The scatter in the data density plots is reduced, but otherwise Fig. 3 is very similar to Fig. 1 and the R^2_{adj} values for the hourly averages in Table 2 are between 0.013 and 0.053 and so are only very marginally larger than for the 1-min data. Fig. 2 is not repeated for hourly means because although the observed distributions are very slightly narrower, so are the fitted ones and the resulting plots are almost indistinguishable from those in Fig. 2.

4. The effect of ionospheric conductivity

An effect that is frequently invoked when considering differences between the electrodynamics of the two ionospheric polar caps is that of ionospheric conductivity. This is a factor for the PCI because, although the algorithm generating the indices makes an allowance for the effect of conductivity, this is only approximate and there will be some residual effects. That this is the case is demonstrated by Fig. 4

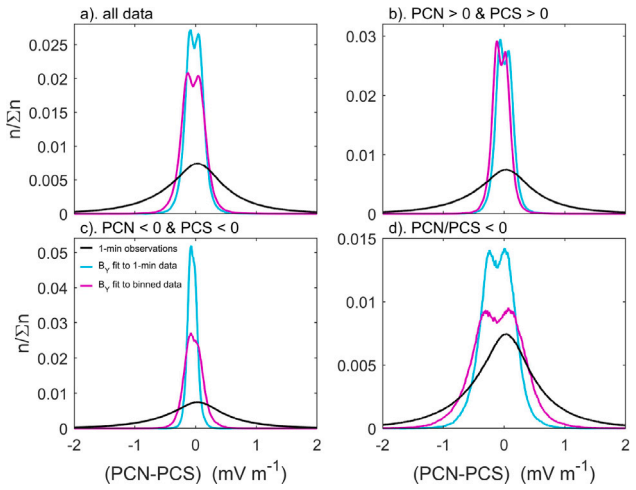

Fig. 2. Distributions of 1-min values of (black lines) observed $(PCN - PCS)$ and of fitted values from the observed (and lagged) IMF Y component in the GSM frame of reference, $[B_Y]_{GSM}$, using the regression fits for 1-min data (cyan lines) and for binned data (mauve lines). (See Table 1 for the regression coefficients). As in Fig. 1, (a) is for all data (1998–2018); (b) when both PCN and PCS are positive; (c) when both PCN and PCS are negative; and (d) when PCN and PCS have opposite polarities. From Table 1, the R^2_{adj} values estimate that the fits to 1-min data (cyan distributions) explain (a) 2.7%, (b) 2.9%, (c) 1.1%, and (d) 5.2% of the observed variation.

which shows variations of mean values with fraction of a calendar year, F, and Universal Time, UT. These $F-UT$ patterns are shown in the top row of the Figure for the two indices and the difference between them. The means are taken in 36 equal-width and equi-spaced bins of F and 24 hourly bins in UT. The top row shows the results for (b) PCN, (c) PCS, and (a) the difference $(PCN - PCS)$.

The bottom panel shows the mean values of the estimated Pedersen conductivities over the Thule and Vostok observing sites respectively, (Σ_{pN} and Σ_{pS}) due to EUV and X-ray solar irradiance. These are computed from the solar zenith angle, χ using the variation of Σ_p with χ given by Ridley et al. (2004). The characteristic pattern reflects the variation of Earth's axial tilt over the year and the diurnal motion of the stations. The peaks near summer and noon predicted in parts (e) and (f) are seen in the PCI in parts (b) and (c), although there is noise and other features are present (notably larger than expected summer midnight values on PCN). These combine to generate the $(\Sigma_{pN} - \Sigma_{pS})$ pattern in part (d) that has distinct similarities to the observed $(PCN - PCS)$ pattern in part (a).

Hence there is undoubtedly a conductivity effect on the difference between PCN and PCS, but Fig. 4 has used averaging which will have greatly reduced the spread of $(PCN - PCS)$ values as did the averaging into IMF $[B_Y]_{GSM}$ bins in the previous section. Figs. 5 and 6 are data density plots for $(PCN - PCS)$ as a function of $(\Sigma_{pN} - \Sigma_{pS})$ for averaging times of $\tau = 1$ min and $\tau = 1$ h, respectively. The mauve and cyan lines are 3rd-order polynomial fits to the 1-min and 1-h values, respectively, and in both plots the $(PCN - PCS) = 0$ line is drawn in white. Note that the $(PCN - PCS)$ scale covers a smaller range in Fig. 6 than in Fig. 5 by a factor of 3. In both figures, the bins used are 0.25 mhos wide in $(\Sigma_{pN} - \Sigma_{pS})$ and 0.25 mV m^{-1} wide in $(PCN - PCS)$ and data are restricted to positive values of both PCS and PCN to avoid complications caused by northward IMF conditions.

The polynomial coefficients and the linear correlation of the polynomial fit to the data with the data are given in the first two columns of Table 3. This table also gives the R^2_{adj} values which show that these modelled conductivity values explain 6.6% of the variation of 1-min values of $(PCS - PCN)$ (when both are positive) and 10.1% of the variation of 1-h averages. These values are higher than for the effect of IMF $[B_Y]_{GSM}$ by a factor of about 2, but are still surprisingly low considering the good agreement of the $F - UT$ plots in parts (a) and (d) of Fig. 4.

This is explained by Fig. 7 which is a scatter plot of the mean values in the 864 $F - UT$ bins that make up the patterns shown in Fig. 4. These points have also been fitted with a third-order polynomial, the coefficients for which are given in the third column of Table 3 and which is plotted as an orange line. Note that the range of the vertical scale has again been decreased and is smaller than that in Fig. 6 by a factor of 5 and smaller than that in Fig. 5 by a factor of 15. The

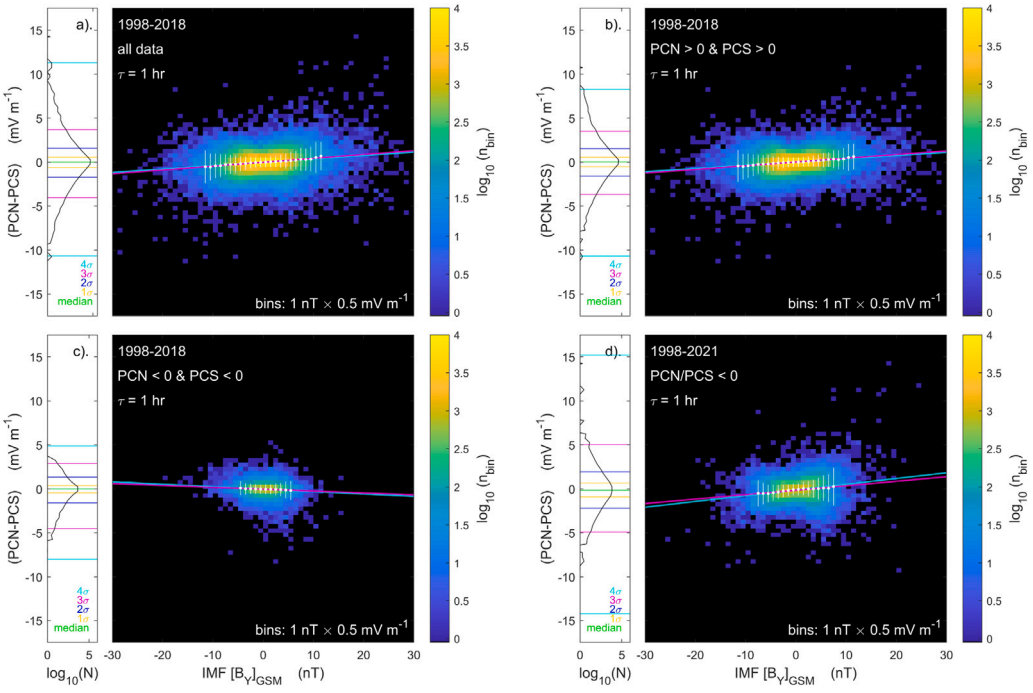

Fig. 3. The same as Fig. 1, for 1-h averages of both the PCI and IMF data ($\tau = 1$ h). The optimum propagation lag of $\delta t = 37$ min for this averaging timescale is employed.

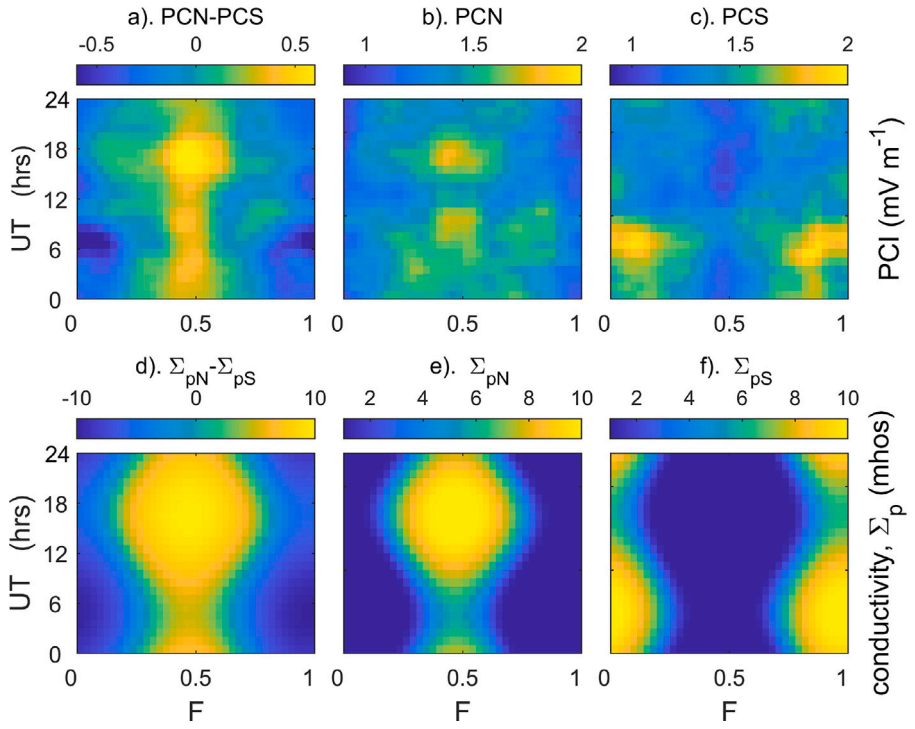

Fig. 4. Fraction of a calendar year (F)–Universal Time (UT) plots illustrating the effect of ionospheric conductivity at the station(s) on ($PCN - PCS$). Mean values are colour-contoured in bins of size ΔUT = 1 h and ΔF = 1/36 yr. The upper row (parts a, b and c) is for the PCI and the lower (parts d, e and f) for the modelled Pedersen conductivities. The left-hand column (a and d) is for the difference between the north and south hemisphere, the middle column (b and e) for the Northern hemisphere and the right-hand column (c and f) is for the southern hemisphere.

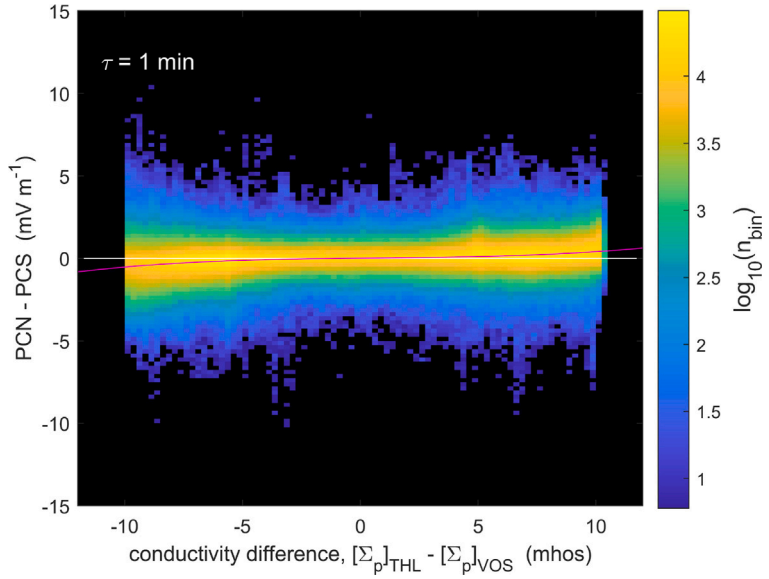

Fig. 5. Analysis of the effect of modelled ionospheric Pedersen conductivity difference ($\Sigma_{pN} - \Sigma_{pS}$) on the difference between the Polar Cap Indices, ($PCN - PCS$), for 1-min data (τ = 1 min). The plot is for data from 1998–2018 when both PCN and PCS are positive. The colour plot is a data density plot (two dimensional histogram) in which the logarithm (to base 10) of the number of samples in each bin n_{bin} is colour coded for bins that are 0.25 mhos wide in ($\Sigma_{pN} - \Sigma_{pS}$) and 0.25 mV m^{-1} wide in ($PCN - PCS$). The mauve line is the optimum 3rd-order polynomial fit to the 1-min data (see Table 3 for details). The white line is ($PCN - PCS$) = 0.

mauve line shows the best fit polynomial from Fig. 5 and the cyan line is that from Fig. 6. The agreement of the three fits is very good, showing that the averaging has had almost no effect on the optimum fit, and that it is the scatter in the ($PCS - PCN$) data that is reduced by the averaging. Table 3 shows that the R^2_{adj} value is considerably increased by the reduced scatter, such that 75.3% of the variation in these binned ($PCS - PCN$) averages is explained by the correspondingly-binned conductivity difference: this is consistent with the level of agreement apparent from a visual inspection of the left-hand column of Fig. 4. Fig. 7 demonstrates that the $F - UT$ patterns shown in Fig. 4 are consistent with the effect of ionospheric conductivity on the PCI, seen in Figs. 5 and 6.

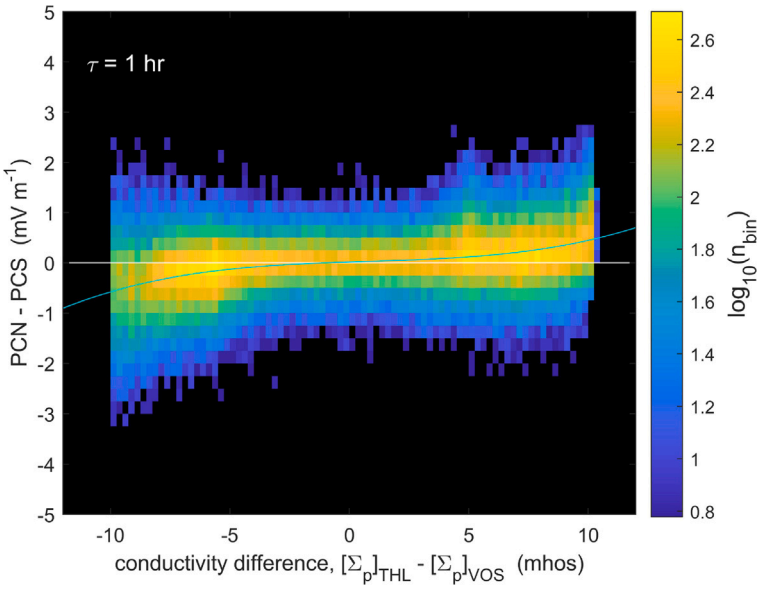

Fig. 6. The same as Fig. 5 for hourly averages (τ = 1 h). The optimum 3rd-order polynomial fit is shown by the cyan line (see Table 3 for details). Note that the vertical, ($PCN - PCS$), scale covers a smaller range than that in Fig. 5.

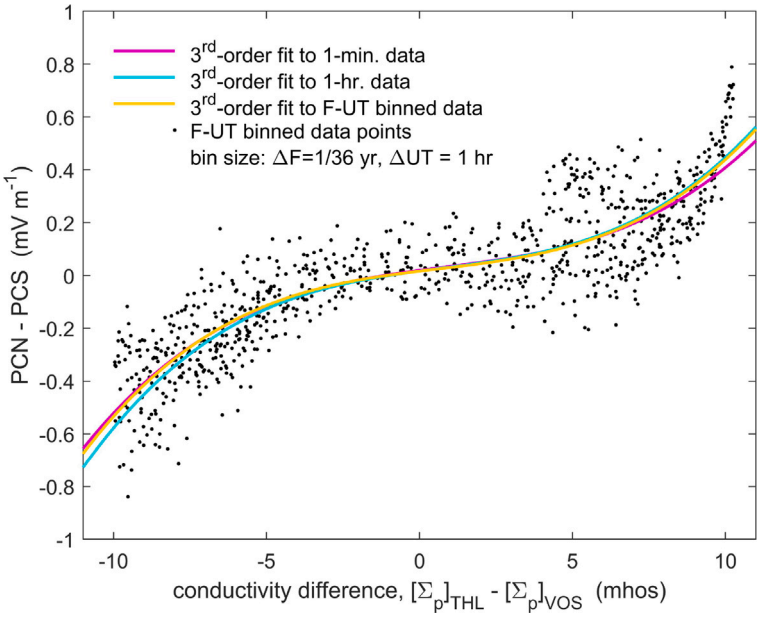

Fig. 7. Scatter plot of bin averages of ($PCN - PCS$) (from Fig. 6a) against the corresponding averages of ($\Sigma_{pN} - \Sigma_{pS}$) (from Fig. 6d). The orange line is the 3rd-order polynomial fit to these data. Also shown are the lines fitted to 1-min values (mauve line, as shown in Fig. 4) and to hourly means (cyan line, as shown in Fig. 5). Note that the vertical, ($PCN - PCS$), scale covers a smaller range than in Figs. 4 and 5.

5. The behaviour of $F - UT$ patterns of the differences between the PCI

In this section we look at the F–UT patterns for the two polarities of IMF $[B_Y]_{GSM}$ and the three subsets of the data: (1) both indices positive ($PCN > 0$, $PCS > 0$); (2) both indices negative ($PCN < 0$, $PCS < 0$); and (3) one index positive, the other negative ($PCN/PCS < 0$).

In interpreting the F–UT patterns, an important factor is that Lockwood and Milan (2023) and Lockwood (2023) have shown that the PCI are strongly modulated by the Russell–McPherron effect (Russell and McPherron, 1973). This effect is caused by the tilt axis of the geomagnetic field which varies with F and UT and means that the large IMF Y-component in the Geocentric Solar Equatorial (GSEQ) reference frame at certain times generates a large southward (negative Z) component in the Geocentric Solar Magnetospheric (GSM) frame, $[B_Z]_{GSM}$, which enhances solar wind magnetosphere coupling and the PCI indices. A key test for this effect is to sort data by the polarity of the IMF Y-component in GSEQ, $[B_Y]_{GSEQ}$: positive values give peak coupling around $10UT$ at the September equinox (F = 0.73) and negative values give peak coupling around $23UT$ at the March equinox (F = 0.22). Because the response to the $[B_Z]_{GSM}$ component of the IMF is not well reproduced by a simple half-wave-rectification function, there is considerable cancellation of the R-M effect if both $[B_Y]_{GSEQ}$ polarities are considered together. Separating them is therefore the key test for the R-M mechanism (Zhao and Zong, 2012; Lockwood et al., 2020a). Using this test, Lockwood and Milan (2023) and Lockwood (2023) have shown that both the PCI Indices are respond strongly to the R-M mechanism.

Table 3
Correlations between $(PCN - PCS)$ and the modelled Pedersen conductivity difference, $(\Sigma_{pN} - \Sigma_{pS})$, computed from the solar zenith angle χ, for 1-min values ($\tau = 1$ min), hourly means ($\tau = 1$ h) and averaged into $F - UT$ bins. Only positive PCS and PCN datapoints are used.

Dataset	PCN > 0, PCS > 0	PCN > 0, PCS > 0	PCN > 0, PCS > 0
averaging	$\tau = 1$ min	$\tau = 1$ h	$F - UT$ bins[a]
figure	4	5	7
number of samples, N	7 352 437	104 561	864
correlation coefficient, R	0.257	0.3062	9.868
p-value for null hypothesis, p	$<10^{-20}$	$<10^{-20}$	$<10^{-20}$
adjusted R^2, R^2_{adj}	0.066	0.101	0.753
r.m.s. fit residual, Δ_{rms} (mV m^{-1})	0.804	0.707	0.133
polynomial[b] coefficient a (mV m^{-1} mho s^{-3})	3.097×10^{-4}	3.562×10^{-4}	3.437×10^{-4}
polynomial[b] coefficient b (mV m^{-1} mho s^{-2})	-7.604×10^{-4}	-8.214×10^{-4}	-6.389×10^{-4}
polynomial[b] coefficient c (mV m^{-1} mho s^{-1})	0.0155	0.0156	0.0142
polynomial[b] coefficient d (mV m^{-1})	0.0193	0.0166	0.0162

[a] bin widths $\Delta F = (1/36)$ yr, $\Delta UT = 1$ h.
[b] Third order polynomial fit $(PCN - PCS)_{fit} = a\Sigma_p^3 + b\Sigma_p^2 + c\Sigma_p + d$.

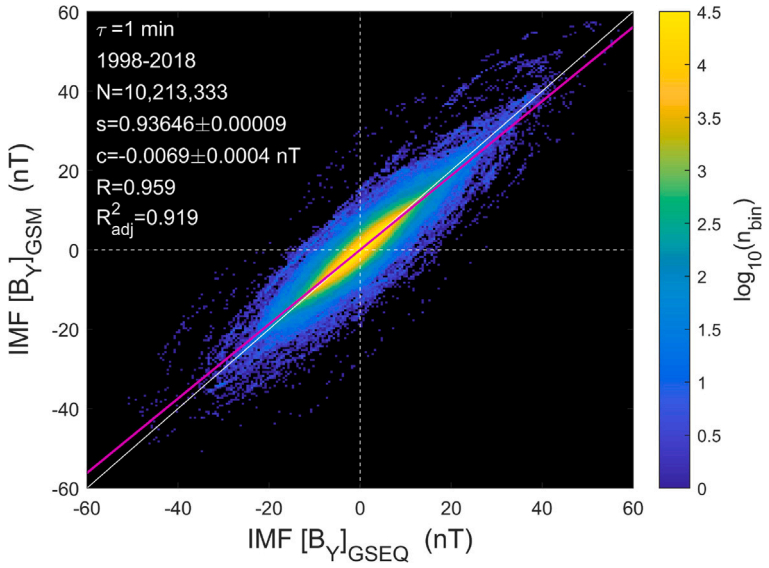

Fig. 8. Data density plot of the IMF B_Y component in the GSM frame as a function of that in the GSEQ frame from Omni data for 1998–2018. Given on the plot are the Number of samples N, the linear correlation coefficient, R and R^2_{adj} and the slope and intercept of the linear regression. The white line is $[B_Y]_{GSM} = [B_Y]_{GSEQ}$ and the mauve line is the optimum linear regression.

On the other hand, the effect on PCI described by Troshichev et al. (2023) depends on the Svalgaard–Mansurov effect and the DP-4 current system and so on the IMF Y-component in the GSM frame, $[B_Y]_{GSM}$. Hence we need to look at the relationship of $[B_Y]_{GSM}$ and $[B_Y]_{GSEQ}$ to understand how much the R-M effect is influencing the analysis of the effects of IMF $[B_Y]_{GSM}$. This is done in Fig. 8 for the interval studied in this paper.

Fig. 8 shows that there is a strong relationship between $[B_Y]_{GSM}$ and $[B_Y]_{GSEQ}$, which is not surprising as the rotation angle between the two frames (around their common X-axis) is between −40° and +40°. The spread around the diagonal white line in Fig. 8 is the effect of the dipole tilt. Hence there is a strong influence of $[B_Y]_{GSEQ}$ on $[B_Y]_{GSM}$. The dashed vertical and horizontal white lines in Fig. 8 are for $[B_Y]_{GSEQ} = 0$ and $[B_Y]_{GSM} = 0$, respectively, and divide the plot into 4 quadrants. Of the $N = 10{,}213{,}333$ valid sample pairs, a total of 9,560,121 (93.6%) are in the two quadrants for which the polarities of $[B_Y]_{GSEQ}$ and $[B_Y]_{GSM}$ are the same and 653,212 are in the other two quadrants for which the polarities are the opposite (6.4%). Hence sorting the data by the polarity of $[B_Y]_{GSM}$ will be similar in effect to sorting by the polarity of $[B_Y]_{GSEQ}$ and we would expect to see the R-M effect and its $F - UT$ pattern. However, the 6.4% of data in the two opposite-polarity quadrants will disrupt this pattern to some degree.

5.1. Anti-sunward convection in both polar caps

The $F-UT$ patterns for $PCN > 0$ and $PCS > 0$ are shown in Fig. 9. This situation arises most strongly when the IMF points southward ($[B_Z]_{GSM} < 0$) and ionospheric convection is antisunward in both polar caps. The upper row of the figure is for $[B_Y]_{GSM} > 0$ and the lower for $[B_Y]_{GSM} < 0$. The patterns for PCN and PCS (middle and right-hand columns) do indeed show elements of the R-M pattern with evidence for September equinox peaks around $10UT$ for $[B_Y]_{GSM} > 0$ and March equinox peaks around $23UT$ for $[B_Y]_{GSM} < 0$. However, the pattern is considerably less clear than for the $[B_Y]_{GSEQ}$ sort of the same data shown in Figure 11 of Lockwood and Milan (2023) and Figure 12 of Lockwood (2023) and hence there is a considerable effect of the difference between $[B_Y]_{GSM}$ and $[B_Y]_{GSEQ}$ that is highlighted in Fig. 8.

The left-hand column of Fig. 9 shows the $F - UT$ patterns of the difference $(PCN - PCS)$. The lower of these two plots, for $[B_Y]_{GSM} < 0$, shows the pattern that we would expect for conductivity effects (shown in Fig. 4d). However, the upper panel (a) for $[B_Y]_{GSM} > 0$ does not show this pattern at all, looking, if anything, like the pattern but inverted in the UT dimension. As the conductivity effects alone would not depend on IMF $[B_Y]_{GSM}$, it is clear that there causes of the patterns are more complex than just conductivity effects.

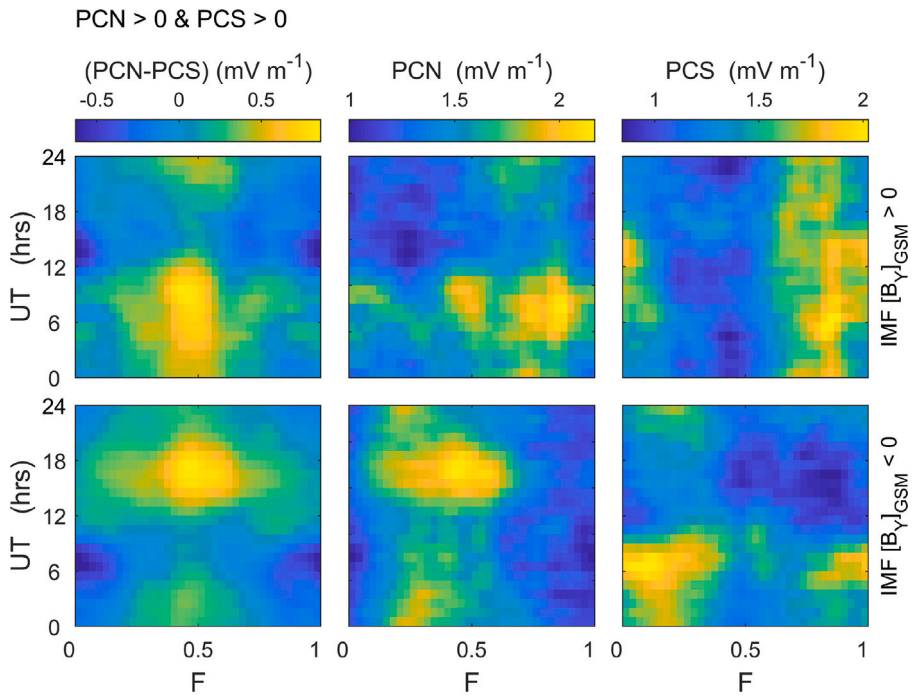

Fig. 9. $F-UT$ plots of PCI for times when both PCN and PCS are positive, sub-divided by the polarity of the IMF Y component in the GSM frame. The upper row is for $[B_Y]_{GSM} > 0$ and the lower row for $[B_Y]_{GSM} < 0$. The left-hand column is for $(PCN - PCS)$, the middle column for PCN and the right-hand column for PCS.

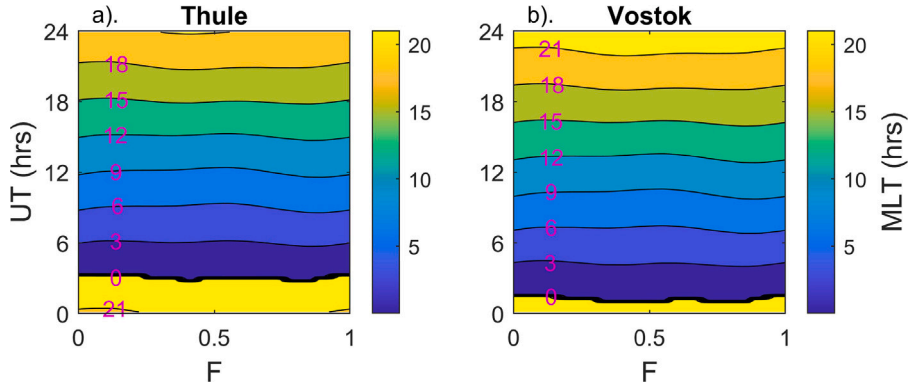

Fig. 10. The magnetic local time (MLT) of the (left) Thule and (right) Vostock stations as a function of F and UT. The values are calculated for 2008, the middle year of the interval of the data used in this study and the computation is as described by Lockwood (2023).

A feature that is seen in all the plots in Fig. 9 for PCN and PCS is a tendency for the R-M equinox peak to extend into the adjacent summer. Section 3 showed that the ,magnitude of the difference between PCN and PCS grows with $|[B_Y]_{GSM}|$ with PCN increased by $[B_Y]_{GSM} > 0$ and PCS increased by $[B_Y]_{GSM} < 0$. Hence in both cases, the indices are increased when the fast antisunward polar cap convection channel is pulled towards dawn (i.e. towards 06 Magnetic Local Time, MLT) by the field line curvature ("tension") force on newly-opened field lines: in other words, by the Svalgaard–Mansurov effect. Note that, where Troshichev et al. (2023) used a description of this IMF B_Y effect in terms of the DP-4 E-region current system, this paper uses the equivalent description in terms of the dawn–dusk asymmetry in the corresponding antisunward F-region flow. The extension of the R-M peaks towards summer reflects the combination of the effects on the PCI of enhanced polar cap electric field and enhanced ionospheric conductivity.

Lockwood (2023) presents a procedure for computing MLT for the stations and Fig. 10 shows the results as a function of F and UT. The plots show that Thule is near dawn (06 h MLT) at around 09 h UT whereas Vostok is at this MLT at around 07 h UT. In Fig. 9 the September R-M peak in PCN is extended into the summer hemisphere ($F = 0.5$) at around 09 h UT when $[B_Y]_{GSM} > 0$ and the March R-M peak in PCS is extended into the summer hemisphere ($F = 0$ or 1) at 07 h UT when $[B_Y]_{GSM} < 0$. This relationship also holds for when the Svalgaard–Mansurov effect is taking the fast polar cap flow towards the dusk flank of the polar cap but the peak station response is earlier than dusk, being around 14 h MLT: the March peak in PCN is extended into summer ($F = 0.5$) at around 17 h UT for $[B_Y]_{GSM} > 0$ and the September peak in PCS is extended into the summer ($F = 0$ or 1) at around 15 h UT for $[B_Y]_{GSM} < 0$. Hence there is a complex combination of effects occurring with solar zenith angle effect of conductivity combining with the IMF B_Y effects of the R-M effect and the dawn–dusk asymmetry caused by the Svalgaard–Mansurov effect.

This understanding of the $F-UT$ patterns for PCN and PCS explains those for the difference $(PCN - PCS)$ noting that the difference is enhanced by increases in PCN and/or by decreases in PCS.

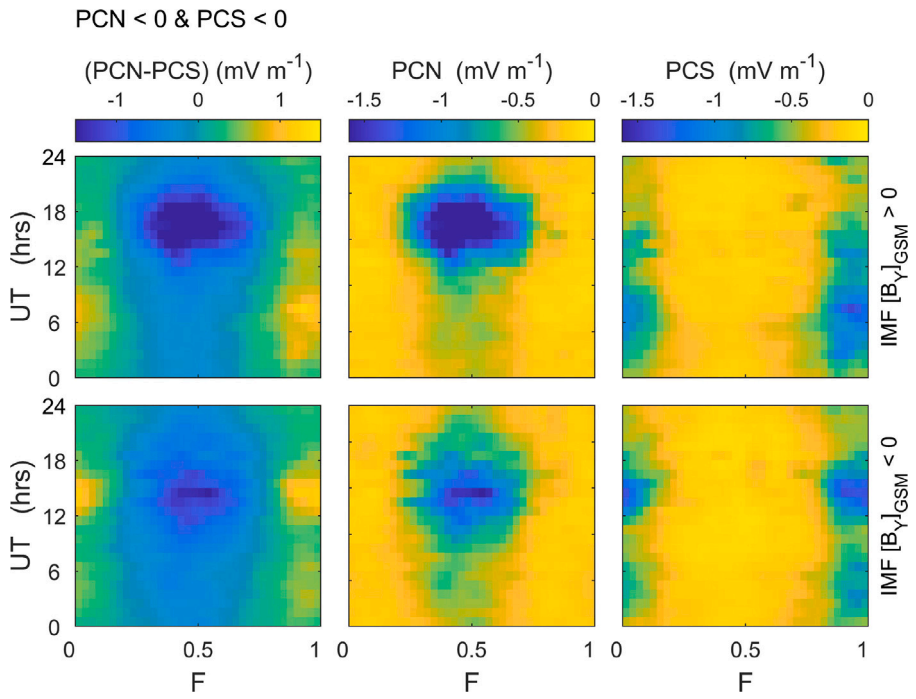

Fig. 11. Same as Fig. 9 for times when both PCN and PCS are both negative.

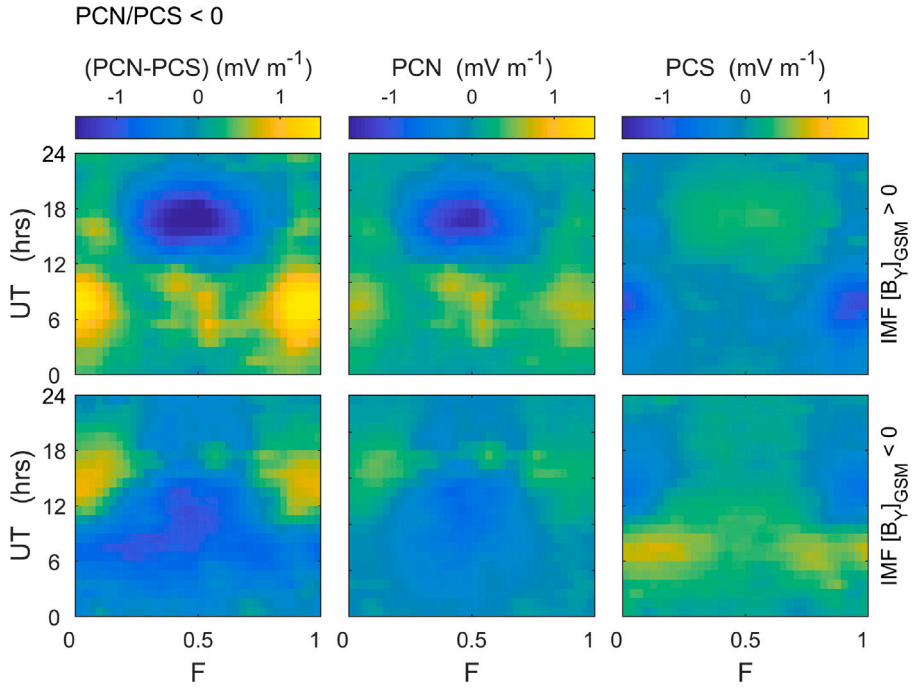

Fig. 12. Same as Fig. 9 for times when PCN and PCS have opposite polarities.

5.2. Sunward convection in both polar caps

When lobe reconnection occurs in both polar caps during northward-IMF conditions, we can see negative values of both PCN and PCS. Lockwood (2023) shows this happens relatively rarely compared to negative values in just one polar cap, discussed below in Section 5.3.

Fig. 11 shows the $F - UT$ patterns for times when $PCN < 0$ and $PCS < 0$. The middle column shows them large negative values in PCN occur in summer (around $F = 0.5$) at around 17 h UT for $[B_Y]_{GSM} > 0$ and around 14 h UT for $[B_Y]_{GSM} < 0$. From Fig. 10 these times correspond to about 14 h MLT and 11 h MLT, a difference that is explained in the schematic presented in Figure 14 of Lockwood (2023). For PCS, negative values are fewer and smaller (see Figure 6 of Lockwood (2023)) but also occur predominantly in summer (around $F = 1$). The UT extent of these negative PCS values is greater than in the northern hemisphere, with the strongest values near 6 h UT for $[B_Y]_{GSM} > 0$ and 14 h UT for $[B_Y]_{GSM} > 0$. From Fig. 10 these times correspond to about 7 and 13 h MLT. This shift is again explained by Figure 14 of Lockwood (2023). Therefore the differences between PCN and PCS in this case are largely due to the IMF $[B_Y]_{GSM}$ effects on the lobe convection cell, as described by Stubbs et al. (2001)

and many other papers (see reviews by Cowley et al. (1991), Cowley and Lockwood (1992) and Lockwood and McWilliams (2021b) and references therein).

5.3. Sunward convection in one polar cap

A number of studies have found that during northward IMF, the more common situation is sunward convection in one polar cap: this is reflected in the negative PCI values (Lockwood, 2023). The $F-UT$ patterns for this situation are shown in Fig. 12. To a considerable extent the patterns for PCS are inversions of those for PCN and so the patterns for $(PCS-PCN)$ are amplified versions of those for PCN. The summer peaks in sunward convection are at the same times as in the case of sunward convection seen in both polar caps discussed in Section 5.2. Hence the differences between PCS and PCN in this case is largely caused by the fact that lobe reconnection is occurring in one polar cap but not the other.

6. Discussion and conclusions

Data density plots of PCN against PCS have been presented by Lockwood (2023). Table 4 gives the number of samples, N, the correlation coefficients R, the R^2_{adj} values and the r.m.s. difference between simultaneous values for the two polar caps in the same four categories as Table 1 and for both 1-min values and hourly means.

It can be seen that for one polar cap giving negative values (19.3% of available 1-min data and 17.5% of hourly means) the correlation and the R^2_{adj} value is very low. We would expect this as most of these cases will be during northward IMF with lobe reconnection dominating in one hemisphere. Such lobe "stirring" reconnection sites have no magnetic connection to the other polar cap and hence no influence on it. Hence the low correlation R and the very small fraction of the variability in one polar cap that is explained by that in the other, R^2_{adj}. This is also true in the relatively small number of cases (8.6% of 1-min data and 7.2% of hourly means) for which PCI values in both hemispheres are negative. In these cases, it is possible that the lobe reconnections driving negative values influence completely different field lines (independent lobe stirring in the two hemispheres) and even when the two reconnections are re-closing open flux by reconnecting the same field lines, they are likely to do so at different times and so there will be differences in the ionospheric response in the two polar caps. Hence the low values of R and R^2_{adj} are again expected.

In this section, we mainly discuss the difference of the two indices when both are positive. Note that this applies to 71.2% of the available 1-min samples and 75.2% of the hourly means. These values are larger than the 50% of time that the IMF is southward and so will contain times when one or both indices are recording antisunward flow that may be part of a northward-IMF lobe reconnection flow cell. To try to reduce, if not eliminate, this possibility, Table 5 reproduces the $PCN>0$, $PCS>0$ column of Table 4 for southward IMF only ($[B_Z]_{GSM}\le 0$). This does raise the correlation coefficient slightly for 1-min values and the R^2_{adj} value is raised from 0.660 to 0.687. Thus the effect of lobe reconnection on positive PCI values was explaining about 2.7% of the covariance. For hourly means there was no significant change.

From Table 5, 69% of the variation in one PCI is consistent with the variation in the other when southward IMF is giving positive values in both polar caps. Most of the remainder of this discussion is aimed at explaining the 31% of the variation in one polar cap index that is not reflected in the other. This figure roughly applies to both 1-min and 1-h averages.

A large number of physical reasons why the simultaneous PCN and PCS values differ have been discussed in this paper. When the IMF is northward, these are largely because of reconnection only occurring in one polar cap. However, in the less-common case of dual reconnection taking place in both polar caps there are differences induced by the B_Y component of the IMF and the sense of circulation in the convection cells induced by the lobe reconnections (Lockwood, 2023).

The more complex situation is when the IMF points southward. The Russell–McPherron (R-M) (Russell and McPherron, 1973) influences the voltage of reconnection between the draped interplanetary magnetic field in the magnetosheath and the geomagnetic field, and because of Maxwell's equation $\nabla\cdot\vec{B}=0$, this influences both polar caps. Hence the R-M effect alone cannot be a direct cause of difference between PCN and PCS. However, it causes a variation in the reconnection voltage with time-of-year F and time-of-day UT that allows other effects to generate differences.

The present paper confirms the effect on $(PCN-PCS)$ of the Y-component of the IMF in the GSM frame discussed by Troshichev et al. (2023). However, it has also shown that this explains just 3% of the variation in 1-min values of $(PCN-PCS)$ when both PCN and PCS are positive. This increases to 4% for hourly means. Hence this effect contributes only about a tenth of the 31% of the variation in one polar cap index that is not reflected in the other during southward IMF, and so is not the major factor.

A second factor is the ionospheric conductivity in the polar cap. It has been shown that this explains close to 7% of the variation in these 1-min values of $(PCN-PCS)$, which rises to 10% for hourly means. Thus the regular EUV-induced ionospheric conductivity difference between the poles can explain of order one third of the variation in one polar cap index that is not matched by the other. We should note that this figure does not include transient changes due to flares and/or SEP events.

Consequently, about 20% of the variation in 1-min. values of $(PCN-PCS)$ during southward IMF remains unexplained by these two factors. For 1-h values this falls to about 15%. This is despite the fact that if we average the data in the right way, both these factors can, on their own, explain or order 90% of the variation.

Lockwood (2023) has argued that the missing factor is induction effects caused by changes in the magnetospheric tail lobe field and/or the magnetosheath field. This cannot be readily quantified because there is no simple metric of the effect. Nevertheless, application of Faraday's induction law shows us how significant a factor this is.

The expectation that PCN and PCS should be the same is essentially a steady-state one. In steady state, the rate of change of the magnetic field is zero which means, by Faraday's law, that the integral of electric field around any loop in space is zero. Consider a loop formed by the polar cap diameter in the ionosphere, along the open field lines that connect those points to the solar wind and which closes in the solar wind. In the absence of significant electrostatic field-aligned voltage, the voltage across the polar cap Φ_{PC} in steady-state must equal that across the segment of the loop in interplanetary space, which is synonymous with the rate of magnetic flux transfer in the solar wind from the dayside to the tail, Φ_{SG}. Furthermore there is no expansion nor contraction of the open polar cap in steady state and so the rate of flux opening by reconnection in the dayside magnetopause Φ_D must equal the rate of flux closure by reconnection in the cross-tail current sheet, Φ_N and also the rate of flux transport between the two (Φ_{PC} in the polar cap and Φ_{SG} in interplanetary space). Hence all these voltage are equal in steady state and the transpolar voltage applied to the northern polar cap Φ_{PCN} must equal that across the southern Φ_{PCS}. Studies have shown that the polar cap indices correlate best with the transpolar voltage (Ridley and Kihn, 2004; Lockwood, 2023) and so steady-state demands that the main differences between PCN and PCS are those associated with conductivity effects (Ridley et al., 2004) and IMF B_Y effects. Hence the expectation that PCN and PCS be the same is essentially a steady-state view and does not apply in general.

The major reason why these voltages can differ is non-steady changes in the magnetospheric and/or magnetosheath magnetic field, dB/dt. This is the third of the three central tenets of the Expanding–Contracting Polar Cap (ECPC) model of ionospheric convection excitation (Cowley and Lockwood, 1992) that has explained observed

Table 4
Correlations between PCN and PCS and for 1-min samples (τ = 1 min) and hourly means (τ = 1 h).

Dataset	All data	PCN > 0, PCS > 0	PCN < 0, PCS < 0	PCN/PCS < 0
1-MINUTE DATA				
Number of samples, N	10,321,808	7,352,443	886,233	1,990,079
% of available data, $100N/\Sigma_N$	100.00	71.23	8.59	19.28
correlation coefficient,	0.787	0.812	−0.034	−0.406
p-value for null hypothesis, p	$<10^{-20}$	$<10^{-20}$	$<10^{-20}$	$<10^{-20}$
adjusted R^2, R^2_{adj}	0.619	0.660	0.001	0.165
r.m.s. difference, Δ_{rms} (mV m^{-1})	0.901	0.832	0.742	1.183
HOURLY MEANS				
number samples, N	162,538	122,282	11,772	28,480
% of available data, $100N/\Sigma_N$	100.00	75.23	7.24	17.52
correlation coefficient, R	0.814	0.833	−0.069	−0.384
p-value for null hypothesis, p	$<10^{-20}$	$<10^{-20}$	7.73×10^{-14}	$<10^{-20}$
adjusted R^2, R^2_{adj}	0.663	0.694	0.005	0.148
r.m.s. difference, Δ_{rms} (mV m^{-1})	0.794	0.736	0.673	1.039

Table 5
Correlations between positive PCN and PCS and for 1-min samples (τ = 1 min) and hourly means (τ = 1 h) when the IMF is southward ($[B_Z]_{GSM} \leq 0$).

Dataset	PCN > 0, PCS > 0 $[B_Z]_{GSM} \leq 0$
1-MINUTE DATA	
Number of samples, N	4,241,962
% of available data, $100N/\Sigma_N$	41.10
correlation coefficient,	0.829
p-value for null hypothesis, p	$<10^{-20}$
adjusted R^2, R^2_{adj}	0.687
r.m.s. difference, Δ_{rms} (mV m^{-1})	0.853
HOURLY MEANS	
number samples, N	62,177
% of available data, $100N/\Sigma_N$	38.92
correlation coefficient, R	0.838
p-value for null hypothesis, p	$<10^{-20}$
adjusted R^2, R^2_{adj}	0.697
r.m.s. difference, Δ_{rms} (mV m^{-1})	0.762

features on ionospheric convection, as discussed in a recent review by Lockwood and Cowley (2022) and demonstrated by a very large number of studies using different datasets (Lockwood et al., 2006a; Milan, 2013; Coxon et al., 2014; Lockwood and McWilliams, 2021b; Milan et al., 2021; Grocott et al., 2023). The three tenets are (1) the continuity of open flux (Holzer et al., 1986), (2) the effect of moving "adiaroic" (non-reconnecting) polar cap boundaries on (the incompressible) ionospheric flow (Siscoe and Huang, 1985), and (3) the inductive decoupling of solar wind and magnetospheric electric fields and voltages in non-steady conditions (Lockwood and Cowley, 1992; Lockwood and Milan, 2023; Lockwood and Morley, 2004). Note that inductive decoupling of electric field and voltages is also a central tenet of the theory of substorms as positive and then negative dB/dt in the tail lobe is what gives energy storage and release in substorm growth and expansion phases (Caan et al., 1973, 1978; McPherron et al., 1993). The decoupling of solar wind and ionospheric voltages is reproduced by simulations by numerical MHD models of the magnetosphere (Connor et al., 2014; Lockwood et al., 2020b; Gordeev et al., 2011).

The inductive decoupling is illustrated by Figure 3 of Lockwood and Milan (2023). In simple terms, the bending of open field lines means that antisunward flux transport rate of open field lines in the solar wind at any one instant does not have to match that in the polar cap, although it will when averaged over long intervals. This means $\Phi_{SG} > \Phi_{PC}$ in substorm growth phases but $\Phi_{SG} < \Phi_{PC}$ in expansion/recovery phases. Unfortunately, there is no simple metric of the hemispheric difference in these inductive decoupling effects that is routinely available and can be used to evaluate their contribution to the difference between the PCI indices directly. However, we can make a first-order calculation of the possible magnitude of the effects seen in case studies. For example, the study of a geomagnetic storm by Lockwood et al. (2023) shows a prolonged growth of the polar cap flux from 0.27 GWb to 1.03 GWb in 6.5 h, an average voltage of $(\Phi_D - \Phi_N) = 32.5$ kV. During this interval the average transpolar voltage $\Phi_{PC} \approx (\Phi_D + \Phi_N)/2$ is of order 30 kV initially rising to 90 kV. Hence the change in tail lobe flux is causing an inductive decoupling that is initially 100% of the transpolar voltage, falling to 33% as the polar cap grows. Other studies reveal even larger fractional changes (Milan et al., 2003). The study by Milan et al. (2021) covers a whole year of data and in phases of polar cap growth (287 substorm growth phases, or start phases of driven convection, and steady convection intervals) in which the average polar cap flux rises from about 0.3 GWb to 0.5 GWb in roughly one hour, giving an inductive voltage of 55 kV. In these intervals, the average transpolar voltage rises from about 2 kV to about 20 kV. Hence the inductive voltages can be many times larger than the transpolar voltage. Differences in PCI would be associated with hemispheric differences in the inductive decoupling. The study by Lockwood et al. (2023) looks at hemispheric differences in the transpolar voltages and shows values that are 50% of the average are possible.

Hence attributing the remaining 15%–20% unexplained variability of one PCI relative to the other to inductive effects is entirely plausible. That is not to say that there are not other factors (such as instrumental errors, transient conductivity enhancements and index processing errors). However, it is certainly true to say that the magnitude of inductive effects is so great that instantaneous differences between PCN and PCS cannot be invoked as evidence for any of the other effects.

CRediT authorship contribution statement

M. Lockwood: Conceptualization, Methodology, Software, Manuscript preparation.

Declaration of competing interest

The authors declare the following financial interests/personal relationships which may be considered as potential competing interests: M. Lockwood reports financial support was provided by Science and Technology Facilities Council. M. Lockwood reports financial support was provided by Natural Environment Research Council.

Data employed

The data used in this study are all openly available. The interplanetary data are available from the Physics Data Facility (SPDF) at NASA's Goddard Space Flight Center as the Omni composite from https://omniweb.gsfc.nasa.gov/ow_min.html. The polar cap indices are available from the International Service of Geomagnetic Indices (ISGI) at http://isgi.unistra.fr/data_download.php.

Acknowledgements

The author is grateful to the instrument scientists and engineers who make the datasets employed in this study possible; in particular those at the National Space Institute, Technical University of Denmark (DTU, Denmark) and the Danish Meteorological Institute (DMI, Denmark) for the PCN index and the Arctic and Antarctic Research Institute (AARI, Russian Federation) for the PCS index. He also thanks the staff of the data centres that allow easy access to the data. These include: the Space Physics Data Facility (SPDF) at NASA's Goddard Space Flight Center for the Omni composite of interplanetary observations; the International Service of Geomagnetic Indices (ISGI), France and collaborating institutes for distribution of the polar cap indices. The author is grateful for funding from the United Kingdom Science and Technology Facilities Council (UKRI/STFC) and the United Kingdom Natural Environment Research Council (UKRI/NERC).

Funding

This work is supported by a number of grants: consolidated grants number ST/R000921/1 and ST/V000497/1 from the United Kingdom Science and Technology Facilities Council (UKRI/STFC) and the SWIGS Directed Highlight Topic Grant number NE/P016928/1/ and grant NE/S010033/1 from the United Kingdom Natural Environment Research Council (UKRI/NERC).

References

Barnett, A.G., 2004. Regression to the mean: what it is and how to deal with it. Int. J. Epidemiol. 34 (1), 215–220. http://dx.doi.org/10.1093/ije/dyh299, URL: https://academic.oup.com/ije/article-lookup/doi/10.1093/ije/dyh299.

Borovsky, J., Birn, J., 2014. The solar wind electric field does not control the dayside reconnection rate. J. Geophys. Res. Space Phys. 119 (2), 751–760. http://dx.doi.org/10.1002/2013JA019193, URL: https://agupubs.onlinelibrary.wiley.com/doi/10.1002/2013JA019193.

Caan, M., McPherron, R., Russell, C., 1973. Solar wind and substorm-related changes in the lobes of the geomagnetic tail. J. Geophys. Res. 78 (34), 8087–8096. http://dx.doi.org/10.1029/JA078i034p08087, URL: http://doi.wiley.com/10.1029/JA078i034p08087.

Caan, M., McPherron, R., Russell, C., 1978. The statistical magnetic signature of magnetospheric substorms. Planet. Space Sci. 26 (3), 269–279. http://dx.doi.org/10.1016/0032-0633(78)90092-2, URL: https://linkinghub.elsevier.com/retrieve/pii/0032063378900922.

Connor, H.K., Zesta, E., Ober, D.M., Raeder, J., 2014. The relation between transpolar potential and reconnection rates during sudden enhancement of solar wind dynamic pressure: OpenGGCM-CTIM results. J. Geophys. Res. Space Phys. 119 (5), 3411–3429. http://dx.doi.org/10.1002/2013JA019728, URL: https://agupubs.onlinelibrary.wiley.com/doi/abs/10.1002/2013JA019728.

Cowley, S.W.H., Lockwood, M., 1992. Excitation and decay of solar wind-driven flows in the magnetosphere-ionosphere system. Ann. Geophys. 10, 103–115, URL: https://ui.adsabs.harvard.edu/abs/1992AnGeo..10..103C, ADS Bibcode: 1992AnGeo..10..103C.

Cowley, S.W.H., Morelli, J.P., Lockwood, M., 1991. Dependence of convective flows and particle precipitation in the high-latitude dayside ionosphere on the x and y components of the interplanetary magnetic field. J. Geophys. Res. 96 (A4), 5557–5564. http://dx.doi.org/10.1029/90JA02063, URL: http://doi.wiley.com/10.1029/90JA02063.

Coxon, J.C., Milan, S.E., Clausen, L.B.N., Anderson, B.J., Korth, H., 2014. A superposed epoch analysis of the regions 1 and 2 Birkeland currents observed by AMPERE during substorms. J. Geophys. Res. Space Phys. 119 (12), 9834–9846. http://dx.doi.org/10.1002/2014JA020500, URL: https://onlinelibrary.wiley.com/doi/abs/10.1002/2014JA020500.

Gordeev, E.I., Sergeev, V.A., Pulkkinen, T.I., Palmroth, M., 2011. Contribution of magnetotail reconnection to the cross-polar cap electric potential drop. J. Geophys. Res. Space Phys. 116 (A8), n/a–n/a. http://dx.doi.org/10.1029/2011JA016609, URL: http://doi.wiley.com/10.1029/2011JA016609.

Grocott, A., Walach, M.-T., Milan, S.E., 2023. SuperDARN observations of the two component model of ionospheric convection. J. Geophys. Res. Space Phys. 128 (6), e2022JA031101. http://dx.doi.org/10.1029/2022JA031101, URL: https://agupubs.onlinelibrary.wiley.com/doi/abs/10.1029/2022JA031101.

Holzer, R.E., McPherron, R.L., Hardy, D.A., 1986. A quantitative empirical model of the magnetospheric flux transfer process. J. Geophys. Res. 91 (A3), 3287. http://dx.doi.org/10.1029/JA091iA03p03287, URL: http://doi.wiley.com/10.1029/JA091iA03p03287.

Kan, J.R., Lee, L.C., 1979. Energy coupling function and solar wind-magnetosphere dynamo. Geophys. Res. Lett. 6 (7), 577–580. http://dx.doi.org/10.1029/GL006i007p00577, URL: http://doi.wiley.com/10.1029/GL006i007p00577.

King, J.H., Papitashvili, N.E., 2005. Solar wind spatial scales in and comparisons of hourly wind and ACE plasma and magnetic field data. J. Geophys. Res. 110, A02104. http://dx.doi.org/10.1029/2004JA010649.

Lockwood, M., 2023. Northern and southern hemisphere polar cap indices: To what extent do they agree and to what extent should they agree? J. Geophys. Res.: Space Phys. 128 (7), e2023JA031464. http://dx.doi.org/10.1029/2023JA031464, URL: https://agupubs.onlinelibrary.wiley.com/doi/10.1029/2023JA031464.

Lockwood, M., Cowley, S.W.H., 1992. Ionospheric convection and the substorm cycle. In: Mattock, C. (Ed.), Substorms 1, Proceedings of the First International Conference on Substorms, ICS-1, Vol. ESA-SP-335. European Apace Agency Publications, Noordwijk, The Netherlands, pp. 99–109, Proceedings of First International Conference on Substorms, ICS-1, held at Kiruna, Sweden on 23-27 March 1992.

Lockwood, M., Cowley, S.W.H., 2022. Magnetosphere-ionosphere coupling: Implications of non-equilibrium conditions. Front. Astron. Space Sci. 9, 908571. http://dx.doi.org/10.3389/fspas.2022.908571, URL: https://www.frontiersin.org/articles/10.3389/fspas.2022.908571/full.

Lockwood, M., Lanchester, B.S., Morley, S.K., Throp, K., Milan, S.E., Lester, M., Frey, H.U., 2006a. Modeling the observed proton aurora and ionospheric convection responses to changes in the IMF clock angle: 2. Persistence of ionospheric convection. J. Geophys. Res. 111 (A2), A02306. http://dx.doi.org/10.1029/2003JA010307, URL: http://doi.wiley.com/10.1029/2003JA010307.

Lockwood, M., McWilliams, K.A., 2021a. On optimum solar wind-magnetosphere coupling functions for transpolar voltage and planetary geomagnetic activity. J. Geophys. Res. Space Phys. 126 (12), http://dx.doi.org/10.1029/2021JA029946, URL: https://onlinelibrary.wiley.com/doi/10.1029/2021JA029946.

Lockwood, M., McWilliams, K.A., 2021b. A survey of 25 Years' transpolar voltage data from the SuperDARN radar network and the expanding-contracting polar cap model. J. Geophys. Res. Space Phys. 126 (9), http://dx.doi.org/10.1029/2021JA029554, URL: https://onlinelibrary.wiley.com/doi/10.1029/2021JA029554.

Lockwood, M., Milan, S., 2023. Universal time variations in the magnetosphere. Front. Astron. Space Sci. 10 (9), 1139295. http://dx.doi.org/10.3389/fspas.2023.1139295, URL: https://www.frontiersin.org/articles/10.3389/fspas.2023.1139295/full.

Lockwood, M., Morley, S.K., 2004. A numerical model of the ionospheric signatures of time-varying magneticreconnection: I. ionospheric convection. Ann. Geophys. 22 (1), 73–91. http://dx.doi.org/10.5194/angeo-22-73-2004, URL: https://angeo.copernicus.org/articles/22/73/2004/.

Lockwood, M., Owens, M.J., Barnard, L.A., 2023. Universal Time variations in the magnetosphere and the effect of CME arrival time: Analysis of the February 2022 event that led to the loss of Starlink satellites. J. Geophys. Res. Space Phys. 128 (3), http://dx.doi.org/10.1029/2022JA031177, URL: https://onlinelibrary.wiley.com/doi/10.1029/2022JA031177.

Lockwood, M., Owens, M.J., Barnard, L.A., Haines, C., Scott, C.J., McWilliams, K.A., Coxon, J.C., 2020a. Semi-annual, annual and Universal Time variations in the magnetosphere and in geomagnetic activity: 1. Geomagnetic data. J. Space Weather Space Clim. 10, 23. http://dx.doi.org/10.1051/swsc/2020023, URL: https://www.swsc-journal.org/10.1051/swsc/2020023.

Lockwood, M., Owens, M.J., Barnard, L.A., Watt, C.E., Scott, C.J., Coxon, J.C., McWilliams, K.A., 2020b. Semi-annual, annual and Universal Time variations in the magnetosphere and in geomagnetic activity: 3. Modelling. J. Space Weather Space Clim. 10, 61. http://dx.doi.org/10.1051/swsc/2020062, URL: https://www.swsc-journal.org/10.1051/swsc/2020062.

Lockwood, M., Rouillard, A.P., Finch, I., Stamper, R., 2006b. Comment on "the IDV index: Its derivation and use in inferring long-term variations of the interplanetary magnetic field strength" by Leif Svalgaard and Edward W. Cliver. J. Geophys. Res. 111 (A9), A09109. http://dx.doi.org/10.1029/2006JA011640, URL: http://doi.wiley.com/10.1029/2006JA011640.

Lukianova, R., Troshichev, O., Lu, G., 2002. The polar cap magnetic activity indices in the southern (PCS) and northern (PCN) polar caps: Consistency and discrepancy. Geophys. Res. Lett. 29 (18), 26–1–26–4. http://dx.doi.org/10.1029/2002GL015179, URL: http://doi.wiley.com/10.1029/2002GL015179.

Matzka, J., Troshichev, O., 2014. The polar cap north (PCN) index. http://dx.doi.org/10.11581/DTU:00000057, URL: https://www.space.dtu.dk/wdc/pcn-index.

McCreadie, H., Menvielle, M., 2010. The PC index: review of methods. Ann. Geophys. 28 (10), 1887–1903. http://dx.doi.org/10.5194/angeo-28-1887-2010, URL: https://angeo.copernicus.org/articles/28/1887/2010/.

McPherron, R., Angelopoulos, V., Baker, D., Hones Jr., E., 1993. Is there a near-Earth neutral line? Adv. Space Res. 13 (4), 173–186. http://dx.doi.org/10.1016/0273-1177(93)90331-5, URL: https://linkinghub.elsevier.com/retrieve/pii/0273117793903315.

Menvielle, M., McCreadie, H., Demetrescu, C., 2013. Recommendation #3 - Recommendation by the Task Force: Fully Recommend Endorsement of the PC Index. Technical Report, International Association of Geomagnetism and Aeronomy, IAGA_documentation_20130225.pdf, IAGA 12th Scientific Assembly, Mérida, Yucatán, Mexico.

Milan, S.E., 2013. Modeling Birkeland currents in the expanding/contracting polar cap paradigm. J. Geophys. Res. Space Phys. 118 (9), 5532–5542. http://dx.doi.org/10.1002/jgra.50393, URL: http://doi.wiley.com/10.1002/jgra.50393.

Milan, S.E., Carter, J.A., Sangha, H., Bower, G.E., Anderson, B.J., 2021. Magnetospheric flux throughput in the Dungey cycle: Identification of convection state during 2010. J. Geophys. Res. Space Phys. 126 (2), e2020JA028437. http://dx.doi.org/10.1029/2020JA028437, URL: https://agupubs.onlinelibrary.wiley.com/doi/abs/10.1029/2020JA028437.

Milan, S.E., Lester, M., Cowley, S.W.H., Oksavik, K., Brittnacher, M., Greenwald, R.A., Sofko, G., Villain, J.-P., 2003. Variations in the polar cap area during two substorm cycles. Ann. Geophys. 21 (5), 1121–1140. http://dx.doi.org/10.5194/angeo-21-1121-2003, URL: https://angeo.copernicus.org/articles/21/1121/2003/.

Nielsen, J., Willer, A., 2019. Restructuring and Harmonizing the Code Used to Calculate the Definitive Polar Cap Index. Technical Report, DTU Space, Copenhagen.

Ridley, A.J., Gombosi, T.I., DeZeeuw, D.L., 2004. Ionospheric control of the magnetosphere: conductance. Ann. Geophys. 22 (2), 567–584. http://dx.doi.org/10.5194/angeo-22-567-2004, URL: https://angeo.copernicus.org/articles/22/567/2004/.

Ridley, A.J., Kihn, E.A., 2004. Polar cap index comparisons with AMIE cross polar cap potential, electric field, and polar cap area. Geophys. Res. Lett. 31 (7), n/a–n/a. http://dx.doi.org/10.1029/2003GL019113, URL: http://doi.wiley.com/10.1029/2003GL019113.

Russell, C.T., McPherron, R.L., 1973. Semiannual variation of geomagnetic activity. J. Geophys. Res. 78 (1), 92–108. http://dx.doi.org/10.1029/JA078i001p00092, URL: http://doi.wiley.com/10.1029/JA078i001p00092.

Siscoe, G.L., Huang, T.S., 1985. Polar cap inflation and deflation. J. Geophys. Res. Space Phys. 90 (A1), 543–547. http://dx.doi.org/10.1029/JA090iA01p00543, URL: http://doi.wiley.com/10.1029/JA090iA01p00543.

Sivadas, N., Sibeck, D., 2022. Regression bias in using Solar wind measurements. Front. Astron. Space Sci. 9, 924976. http://dx.doi.org/10.3389/fspas.2022.924976, URL: https://www.frontiersin.org/articles/10.3389/fspas.2022.924976/full.

Stauning, P., 2011. Determination of the quiet daily geomagnetic variations for polar regions. J. Atmos. Sol.-Terr. Phys. 73 (16), 2314–2330. http://dx.doi.org/10.1016/j.jastp.2011.07.004, URL: https://linkinghub.elsevier.com/retrieve/pii/S1364682611001994.

Stauning, P., 2013. The Polar Cap index: A critical review of methods and a new approach. J. Geophys. Res. Space Phys. 118 (8), 5021–5038. http://dx.doi.org/10.1002/jgra.50462, URL: https://onlinelibrary.wiley.com/doi/10.1002/jgra.50462.

Stauning, P., 2021a. The Polar Cap (PC) index combination, PCC: relations to solar wind properties and global magnetic disturbances. J. Space Weather Space Clim. 11, 19. http://dx.doi.org/10.1051/swsc/2020074, URL: https://www.swsc-journal.org/10.1051/swsc/2020074.

Stauning, P., 2021b. Transpolar convection and magnetospheric ring current relations: Real-time applications of the polar cap (PC) indices. Space Weather 19 (7), http://dx.doi.org/10.1029/2020SW002702, URL: https://onlinelibrary.wiley.com/doi/10.1029/2020SW002702.

Stauning, P., 2022a. Reply to comment by troshichev et al. on “the use of invalid Polar Cap South (PCS) indices in publications”. J. Geophys. Res. Space Phys. 127 (10), http://dx.doi.org/10.1029/2022JA030856, URL: https://onlinelibrary.wiley.com/doi/10.1029/2022JA030856.

Stauning, P., 2022b. The use of invalid polar cap south (PCS) indices in publications. J. Geophys. Res. Space Phys. 127 (5), http://dx.doi.org/10.1029/2022JA030355, URL: https://onlinelibrary.wiley.com/doi/10.1029/2022JA030355.

Stubbs, T.J., Lockwood, M., Cargill, P., Fennell, J., Grande, M., Kellett, B., Perry, C., Rees, A., 2001. Dawn-dusk asymmetry in particles of solar wind origin within the magnetosphere. Ann. Geophys. 19 (1), 1–9. http://dx.doi.org/10.5194/angeo-19-1-2001, URL: https://angeo.copernicus.org/articles/19/1/2001/.

Troshichev, O., 2022. PC index as a ground-based indicator of the solar wind energy incoming into the magnetosphere: (1) relation of PC index to the solar wind electric field EKL. Front. Astron. Space Sci. 9, 1069470. http://dx.doi.org/10.3389/fspas.2022.1069470, URL: https://www.frontiersin.org/articles/10.3389/fspas.2022.1069470/full.

Troshichev, O., Andrezen, V., 1985. The relationship between interplanetary quantities and magnetic activity in the southern polar cap. Planet. Space Sci. 33 (4), 415–419. http://dx.doi.org/10.1016/0032-0633(85)90086-8, URL: https://linkinghub.elsevier.com/retrieve/pii/0032063385900868.

Troshichev, O., Dolgacheva, S., Sormakov, D., 2022a. Invariability of relationships between the solar wind electric field e and the magnetic activity indices PC, AL and dst. J. Atmos. Sol.-Terr. Phys. 235, 105894. http://dx.doi.org/10.1016/j.jastp.2022.105894, URL: https://linkinghub.elsevier.com/retrieve/pii/S1364682622000682.

Troshichev, O., Dolgacheva, S.A., Sormakov, D.A., 2022b. Comment on “the use of invalid Polar Cap South (PCS) indices in publications” by Stauning. J. Geophys. Res. Space Phys. 127 (10), http://dx.doi.org/10.1029/2022JA030820, URL: https://onlinelibrary.wiley.com/doi/10.1029/2022JA030820.

Troshichev, O., Janzhura, A., Stauning, P., 2006. Unified PCN and PCS indices: Method of calculation, physical sense, and dependence on the IMF azimuthal and northward components. J. Geophys. Res. 111 (A5), A05208. http://dx.doi.org/10.1029/2005JA011402, URL: http://doi.wiley.com/10.1029/2005JA011402.

Troshichev, O., Stepanov, N., Sormakov, D., 2023. Physical reasons for regular discrepancies in values of the PCN and pcs indices characterizing magnetic activity in the northern and southern polar caps. J. Atmos. Sol.-Terr. Phys. 249, 106096. http://dx.doi.org/10.1016/j.jastp.2023.106096, URL: https://www.sciencedirect.com/science/article/pii/S1364682623000949.

Vasyliunas, V., Kan, J., Siscoe, G., Akasofu, S.-I., 1982. Scaling relations governing magnetospheric energy transfer. Planet. Space Sci. 30 (4), 359–365. http://dx.doi.org/10.1016/0032-0633(82)90041-1, URL: https://linkinghub.elsevier.com/retrieve/pii/0032063382900411.

Vennerstrøm, S., 1991. The Geomagnetic Activity Index PC (Ph.D. Thesis) 91–3. Danish Meteorological Institute, Copenhagen.

Zhao, H., Zong, Q.-G., 2012. Seasonal and diurnal variation of geomagnetic activity: Russell-Mcpherron effect during different IMF polarity and/or extreme solar wind conditions. J. Geophys. Res. Space Phys. 117 (A11), n/a–n/a. http://dx.doi.org/10.1029/2012JA017845, URL: http://doi.wiley.com/10.1029/2012JA017845.